iScience

CellPress
OPEN ACCESS

Article

Co-Cu nanoparticles uniformly embedded in the intra-crystalline mesoporous Silicalite-1 for catalytic ammonia borane hydrolysis

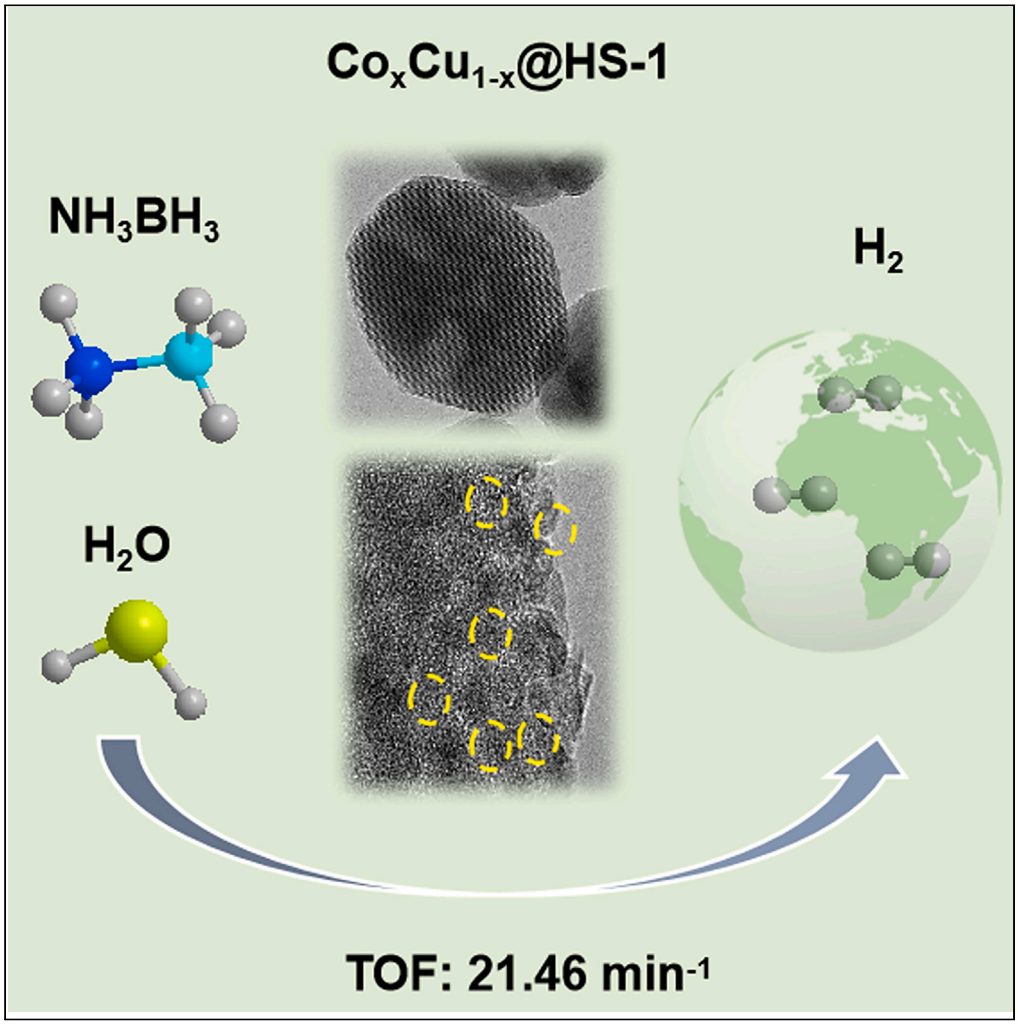

Huijuan Wei, Yanan Cui, Huinan Hou, ..., Xiangyu Wang, Yanyan Liu, Baojun Li

lbjfcl@zzu.edu.cn

Highlights

Co-Cu nanoparticles were embedded in the intracrystalline mesoporous Silicalite-1

TOF of Co_xCu_{1-x}@HS-1 in the ammonia borane hydrolysis was 21.46 $mol_{H2} \cdot mol_{Me}^{-1} \cdot min^{-1}$

Intracrystalline mesopores improved the accessibility of the active sites

The introduction of Cu regulates the electronic properties of Co

Wei et al., iScience *27*, 109745
May 17, 2024
https://doi.org/10.1016/j.isci.2024.109745

iScience

CellPress
OPEN ACCESS

Article

Co-Cu nanoparticles uniformly embedded in the intra-crystalline mesoporous Silicalite-1 for catalytic ammonia borane hydrolysis

Huijuan Wei,[1] Yanan Cui,[1] Huinan Hou,[1] Xiaoguang Zheng,[2] Peng Jin,[2] Yiqiang Wen,[1] Xiangyu Wang,[1] Yanyan Liu,[1,3] and Baojun Li[1,4,*]

SUMMARY

Zeolite-encaged metal nanoparticles (NPs) catalysts are emerging as a new frontier owing to their superior ability to stabilize the structure and catalytic performance in the thermal and environmental catalytic reaction. However, the pore size below 2 nm of the conventional zeolites usually limits the accessibility of metal active sites. Herein, Co-Cu NPs of about 2.5–3.5 nm were uniformly encapsulated in the intracrystalline mesoporous Silicalite-1 (S-1) through alkali-treatment ligand-assisted strategy. The obtained sample (termed Co_xCu_{1-x}@HS-1) exhibited efficient activity and stability in the ammonia borane hydrolysis with the highest TOF value of 21.46 $mol_{H2} \cdot mol_{Me}^{-1} \cdot min^{-1}$. UV–vis DRS spectra indicated that intracrystalline mesopores have greatly improved the openness and accessibility of the active sites, thus improving their catalytic performance. The introduction of Cu regulates the electronic properties of Co, further increasing hydrogen production activity. This research creates new prospects to design other high-performance hierarchical porous zeolite-confined metal/metal oxide catalysts.

INTRODUCTION

Hydrogen energy is one of the most attractive green energy carriers due to high energy density and environment-friendly advantage.[1–5] Ammonia borane (AB) has been recognized to be the most promising candidates for chemical hydrogen storage materials for non-toxicity, higher hydrogen content (19.6 wt%), and excellent stability at room temperature.[6] At present, the effective AB hydrogen production catalysts are mainly divided into noble metals (Ru, Pd, Pt, and Rh) and non-noble metals (Co, Ni, Cu, and Fe).[7–9] Although the precious metals possess very high intrinsic activity with turnover frequency (TOF) up to 10^3 min^{-1}, they are scarce and expensive. Non-precious metals are abundant, cheap, and commonly used as active components in industrial catalysts, but the intrinsic activity is still far from satisfying the requirements of practical applications. To substantially promote the intrinsic activity, the dual metal/site catalysts responsible for the efficient dissociation of O-H in B-H and water molecules have been designed and constructed.[10–14] The refined alteration of active sites in CoP/Co_2P@carbon heterostructure via O modification had been studied to boost the catalytic activity for efficient NH_3BH_3 hydrolysis (turnover frequency, TOF = 35 min^{-1}).[15] The migration and aggregation of bimetallic active site catalysts during the reaction have a negative effect on the catalytic activity. Enhancing the adhesion strength of metal sites on the carrier or spatially isolating metal sites can prevents them from gathering and growing together. Porous materials such as zeolites, carbon, and metal-organic materials (MOFs) are often used to stabilize the active site using their spatial structure and provide molecular reaction channels.[16–20]

Encapsulation of metal nanoclusters or nanoparticles (NPs) into zeolites (metal@zeolite) have attracted extensive attention in recent years due to remarkable promotion in the stability against sintering and unexpected shape selectivity on the basis of zeolites. Recently many strategies for fabricating metal@zeolite have been developed, including ligand-stabilized metal precursors methods,[21–23] mercaptosilane-assisted process,[24,25] bottom-up approaches,[26,27] an interzeolite transformation,[28,29] and a metal-containing zeolite seed-directing crystallization method.[30,31] Nevertheless, there are still existing some limitations such as the molecule diffusion and the metal active sites accessibility for these microporous zeolites confined catalysts because the pore size of the conventional zeolites is usually below 2 nm. A promising conception to resolve these problems is introducing meso or macropores in the zeolite to improve the mass-transfer efficiency and accessibility of the active sites.[32] Honggen Peng et al. have developed a facile two-step *in situ* mesoporogen-free dry-gel conversion method to successfully prepare a single crystal intra-mesopore zeolite encaged Pd NPs.[33] Jing Gu et al. also synthesized Pt NPs encapsulated in the hierarchical ZSM-5 catalysts via a two-step dry-gel conversion approach.[34] The key point of the method is the prefabrication of mesopores in the ZSM-5 zeolites in which the metallic species deposited, followed by coverage with S-1 synthesis gel and recrystallization of the dry-gel by

[1]College of Chemistry, Zhengzhou University, 100 Science Road, Zhengzhou 450001, P.R. China
[2]Henan Shenma Catalytic Technology Co., Ltd., Pingdingshan 467200, P.R. China
[3]College of Science, Henan Agricultural University, 63 Nongye Road, Zhengzhou 450002, P.R. China
[4]Lead contact
*Correspondence: lbjfcl@zzu.edu.cn
https://doi.org/10.1016/j.isci.2024.109745

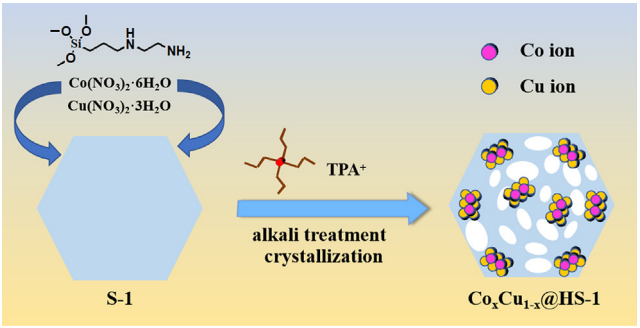

Figure 1. Schematic diagram of the preparation of Co_xCu_{1-x}@HS-1

vapor-phase treatment. The uniform mesoporous structure and the nanosized crystals of the zeolite shell promoted the mass-transfer efficiency and active site accessibility in the above two catalysts. Though there are many strategies to create meso or macro pores in the microporous crystalline zeolites, it remains a challenge to construct single crystal zeolites with intracrystalline mesopores (intra-mesopores) and confine the active metal NPs simultaneously.

In this paper, we developed an alkali treatment ligand-assisted method to encapsulate Co-Cu NPs within the intracrystalline mesoporous S-1 successfully. The key point of our method is combing the ligand-protected strategy with the creation of additional mesopores in the zeolite by alkali treatment. S-1 was first prepared under the hydrothermal condition, then were hydrothermally post-treated with the mixed solution of ethanolamine (ETA), N,N,N-tripropyl-1-propanaminium bromide (TPABr) and N-[3-(trimethoxysilyl)propyl]ethylenediamine (TPE) complexing Co and Cu species. To our delight, compared to the S-1 encaged Co and Cu NPs catalyst by *in-situ* ligand-assisted method, the Co_xCu_{1-x}@HS-1 prepared by the alkali-treatment ligand-assisted method was more efficient in hydrogen production from AB. $Co_{0.9}Cu_{0.1}$@HS-1 show the best catalytic performance with a TOF value of 21.46 $mol_{H2}\cdot mol_{Me}^{-1}\cdot min^{-1}$ at 303 K through the optimization investigation of Co and Cu molar ratio and an excellent stability over six cycles during the NH_3BH_3 hydrolysis reaction.

RESULTS AND DISCUSSION

Catalysts characterization

The designed catalyst was synthesized by desilication-recrystallization process. This is shown in Figure 1. During the synthesis process the zeolite (S-1) was added to the alkali treatment solution and TPE complexing Co and/or Cu metal solution. Then the obtained suspension was crystallized to a mesoporous zeolite-encapsulated metal catalyst. TPE was a bifunctional ligand containing a chelating bidentate amine functionality and an alkoxysilane moiety. During the post-treatment process, S-1 zeolites undergone the desilication and recrystallization. Some Si species of S-1 removed to produce the mesopores, the silicon species in the TPE entered the S-1 framework under the TPA^+ template agent and the metal species are coated in the S-1 simultaneously. Therefore, the catalyst generates some mesopores while ensuring the encapsulation of metal particles. The weight content and molar ratio of Co and Cu in the samples were verified by ICP-OES. The results are shown in Table 1. It showed that the total amount of metal in the catalyst was controlled to 3–5 wt%.

The morphology, size, and elemental distribution of the Co_1Cu_0@S-1 (Figure S1) and $Co_{0.9}Cu_{0.1}$@HS-1 samples were characterized by HRTEM. Figures 2A–2E show that the $Co_{0.9}Cu_{0.1}$@HS-1 maintains the original ellipsoidal morphology of S-1, but there is a large number of intracrystalline mesopores (bright portion in Figures 2A–2E) ranging from roughly 8 to 50 nm. Furthermore, there are some dark spots inside the molecular sieve crystals in Figures 2D–2H. It indicates that the Co and Cu metals are uniformly embedded within the shell layer of the hierarchical pore S-1 and are not encapsulated in the mesoporous cavity. This is due to the partial dissolution of the silicon species of S-1 crystals by alkali etching under hydrothermal conditions, the recrystallization of the silicon species in solution on the surface of the molecular sieve in the presence of TPA+ and encapsulation of the metal species in the S-1 simultaneously. The inset particle size distribution plot in Figure 2E illustrates that the average particle size of Co-Cu metal NPs is approximately 2.7 nm Figures 2F–2H show clear metal lattice stripes. The lattice stripes with a spacing of 0.205 nm might be a combination of the (111) lattice spacing of Cu (0.21 nm) and the (111) crystal plane of Co (0.19 nm).[35,36] Figure 2H shows the spacing of 0.243 nm lattice stripes is due to the (311) crystal plane of Co_3O_4.[37] The elemental mapping of the $Co_{0.9}Cu_{0.1}$@HS-1 catalyst (Figures 2I–2N) shows that the elemental composition of the whole catalyst includes four kind of elements; Co and Cu were uniformly distributed in the hierarchical pore S-1 molecular sieve. Figure S1 shows that about 2.7 nm Co NPs are uniformly embedded within microporous S-1 zeolites and no mesopores are observed.

XRD of Co_xCu_{1-x}@HS-1 and Co_xCu_{1-x}@S-1 are shown in Figures 3A and S2. It can be seen that each sample has a typical MFI characteristic diffraction peak and the introduction of the metal species does not disrupt the topology of S-1. The characteristic diffraction peaks of the Co oxides ($2\theta = 45°$) are not visible in the pattern,[38] this indicates that the metallic Co species encapsulated within the molecular sieve are present in a highly dispersed form corresponding to the metal particle size with 2.5 nm in the TEM. In addition, the characteristic diffraction peak at 43° in $Co_{0.8}Cu_{0.2}$@HS-1, $Co_{0.7}Cu_{0.3}$@HS-1, and $Co_{0.6}Cu_{0.4}$@HS-1 is attributed to copper oxide,[39] and the intensity of this peak increases with Cu content. It provides the proof that some larger Cu oxide particles occur when the Cu: Co molar ratio is above 0.25. In the same neutral aqueous solution, the standard molar Gibbs free energies of Cu ion (64.77 kJ mol^{-1}) is much larger than that of Co ion (−58.2 kJ mol^{-1}),

Table 1. The composition of Co and Cu and textural properties of Co_xCu_{1-x}@HS-1 samples

Sample	Co (wt%)	Cu (wt%)	Molar ratio	Surface area ($m^2 \cdot g^{-1}$)			Pore volume ($cm^3 \cdot g^{-1}$)	
				S_{BET}	S_{Mic}	S_{Ext}	V_{Total}	V_{Mic}
Co@HS-1	4.51	0	–	327	221	106	0.250	0.114
$Co_{0.9}Cu_{0.1}$@HS-1	2.81	0.26	10.8	335	214	121	0.265	0.110
$Co_{0.8}Cu_{0.2}$@HS-1	3.83	0.83	4.61	336	193	143	0.260	0.101
$Co_{0.7}Cu_{0.3}$@HS-1	2.66	0.93	2.86	338	203	135	0.264	0.105
$Co_{0.6}Cu_{0.4}$@HS-1	2.91	1.55	1.88	340	203	137	0.261	0.105

so Cu is more likely to aggregate. Figure 3B shows the N_2 adsorption-desorption isotherms of the Co_xCu_{1-x}@HS-1 samples. The adsorption isotherm types of all samples belong to type IV curves, indicating the presence of microporous structures in the samples. The obvious H1-type hysteresis loops appeared at p/p_0 = 0.4–1.0 illustrate the occurrence of mesopores. The textural properties are shown in Table 1. In comparison with Co_1Cu_0@S-1 and $Co_{0.9}Cu_{0.1}$@S-1 prepared by *in-situ* ligand-assisted method, Co_1Cu_0@HS-1and $Co_{0.9}Cu_{0.1}$@HS-1 sample showed a significant increase in the external surface area and a slight increase in the total surface area. In addition, the total surface area of Co_xCu_{1-x}@HS-1 series samples increased significantly with the increase of Cu content. Co_1Cu_0@HS-1 and $Co_{0.9}Cu_{0.1}$@HS-1 were analyzed by XPS in order to know the chemical states and the electronic structures in Figures 3C and 3D. In both samples, spectra exhibited a doublet of Co $2p_{3/2}$ and Co $2p_{1/2}$ peaks at about 780–785 and 795–801 eV, respectively. The presence of Co ions are also confirmed by intensive "shake-up" satellites at about 787 eV and 804 eV.[40] The value between the maxima of Co $2p_{3/2}$ and Co $2p_{1/2}$ peaks is 15.9 and 16.0 eV for Co_1Cu_0@HS-1 and $Co_{0.9}Cu_{0.1}$@HS-1, respectively. The $Co_{0.9}Cu_{0.1}$@HS-1 negatively shifted by 0.1 eV provided the intrinsic charge redistribution between copper and cobalt element and direct electron-enriched Co. Due to the small amount and confinement inner the $Co_{0.9}Cu_{0.1}$@HS-1, less relevant information can be observed to determine the oxidation state of Cu.

In order to investigate the local environment of Co and Cu in the microporous and mesoporous zeolite, UV–vis DRS spectra of Co_xCu_{1-x}@S-1 and Co_xCu_{1-x}@HS-1 are presented in Figures 3E and 3F. In Figure 3F, the band at 210 nm is attributed to silica framework of S-1. According to the reported literature, tetrahedral Co^{2+} ions are identifiable by the triplet at 540, 580, and 625 nm as found in the compound $CoAl_2O_4$[41,42] and the spectrum of Co_3O_4 was characterized by broad bands at 670 and 380 nm peaks.[43] For Co_xCu_{1-x}@HS-1 series samples, a broad triplet absorption band at 517, 580 and 650 nm exists in the d–d transition region of 500–700 nm. This is a typical characteristic of Co ion complexes, arising from the tetrahedral Co^{2+} (d^7) ground state exhibiting three symmetries and spin-allowed transitions: $\nu_1 = {}^4A_2(F) \rightarrow {}^4T_2(F)$, $\nu_2 = {}^4A_2(F) \rightarrow {}^4T_1(F)$,

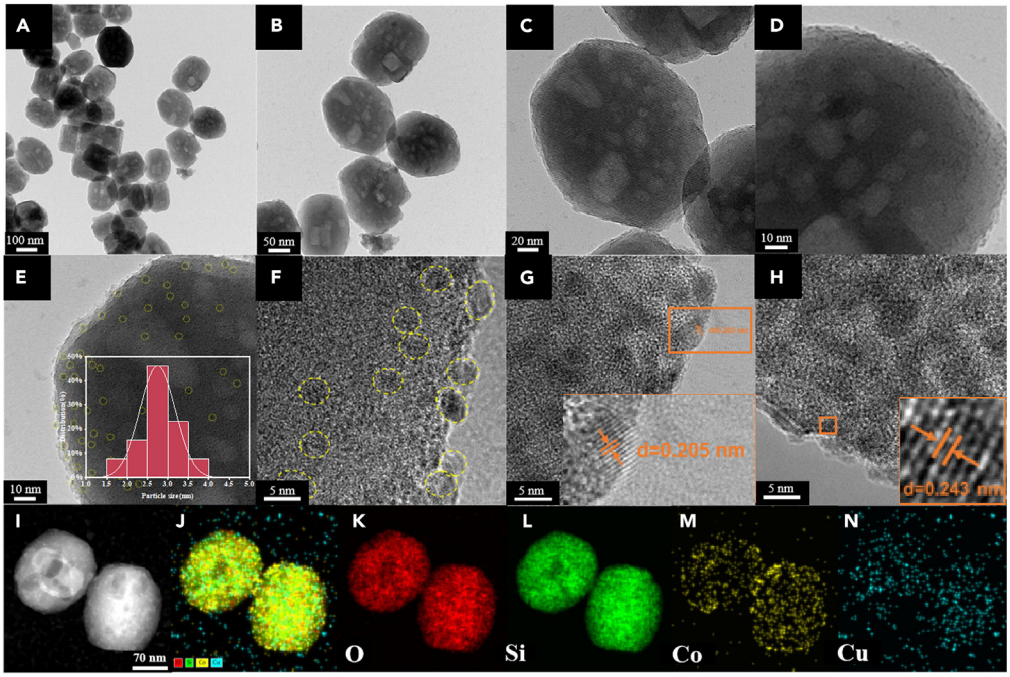

Figure 2. HRTEM and elemental mapping images of $Co_{0.9}Cu_{0.1}$@HS-1 samples

HRTEM images (A–H) and elemental mapping images (I–N) of $Co_{0.9}Cu_{0.1}$@HS-1 samples.

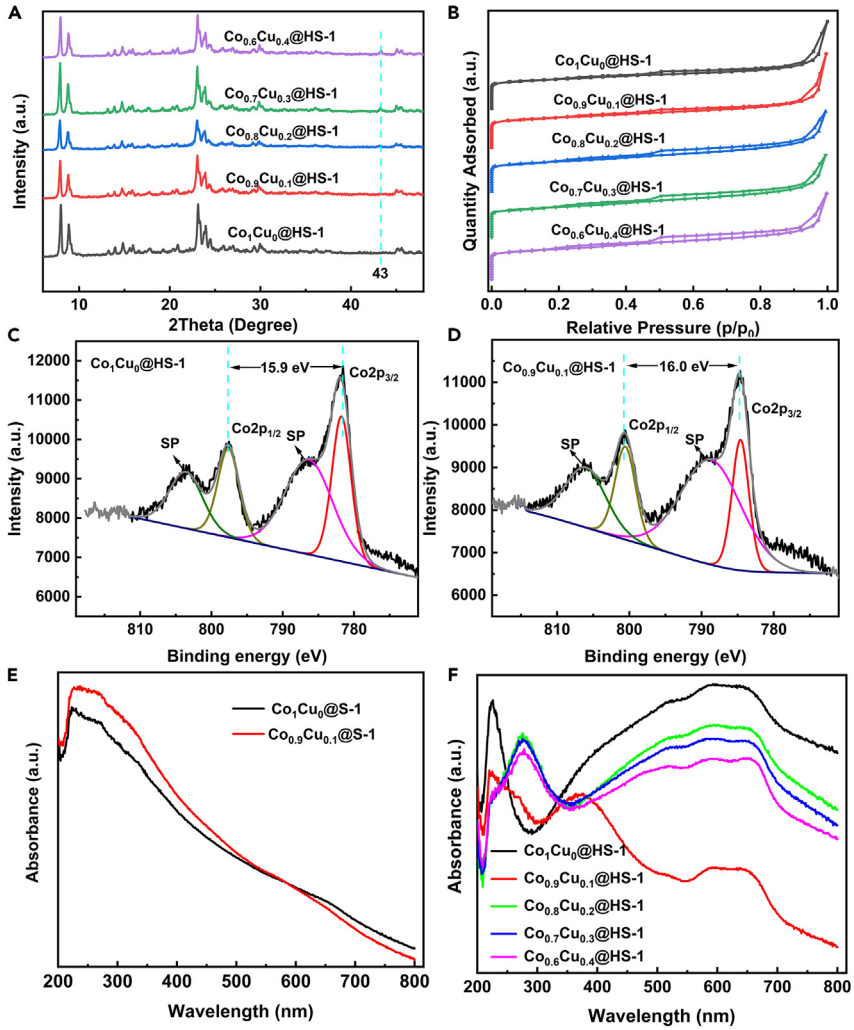

Figure 3. Characterization results of Co_xCu_{1-x}@HS-1 and Co_xCu_{1-x}@S-1 samples

(A) XRD patterns and (B) N_2 adsorption-desorption isotherms of Co_xCu_{1-x}@HS-1 samples.

(C) XPS spectra of Co 2p of Co_1Cu_0@HS-1.

(D) $Co_{0.9}Cu_{0.1}$@HS-1.

(E) UV-vis DRS spectra of Co_xCu_{1-x}@S-1.

(F) UV–vis DRS spectra of Co_xCu_{1-x}@HS-1.

and $\nu_3 = {}^4A_2(F) \rightarrow {}^4T_1(P)$.[44] The band around 650 nm might be a combination of the 670 nm peak of Co_3O_4 and the 625 nm peak of the tetrahedral Co^{2+}. In addition, for $Co_{0.9}Cu_{0.1}$@HS-1 the absorption band at 380 nm assigned to octahedral Co^{3+} (HT) ($^1A_{1g} \rightarrow {}^1T_{2g}$ transition) is much more pronounced. This indicated many Co_3O_4 species existed in the $Co_{0.9}Cu_{0.1}$@HS-1 catalysts, which was in good agreement with TEM results. However, the band in the region of 300–700 nm was barely discernible in the Co_xCu_{1-x}@S-1 samples (Figure 3E), although these samples have comparable cobalt content in comparison with Co_xCu_{1-x}@HS-1. These results indicated that openness and accessibility of the active sites of the metal catalyst confined by molecular sieve can be greatly improved by constructing intracrystalline mesopores.

Catalytic performance

The catalytic activity of various samples and S-1 was evaluated using the hydrolysis of AB. S-1 zeolite has no catalytic activity at all for AB hydrolysis. The Co_1Cu_0@S-1 and $Co_{0.9}Cu_{0.1}$@S-1 samples synthesized by *in-situ* ligand-assisted method showed low activity to hydrogen production of AB (Figure S3). When 45 mg AB was used for the reaction, the maximum hydrogen production was 8 and 20 mL, respectively, far below the stoichiometric hydrogen production value. However, Co_xCu_{1-x}@HS-1 samples exhibited the relatively high hydrogen production capacity and $Co_{0.9}Cu_{0.1}$@HS-1 had the highest TOF value with 21.46 min^{-1} (Figures 4A and 4B). The main reason for the catalytic difference between Co_xCu_{1-x}@S-1 and Co_xCu_{1-x}@HS-1 may be due to the presence of mesopores and the enhanced accessibility of Co active sites in the Co_xCu_{1-x}@HS-1 catalysts.

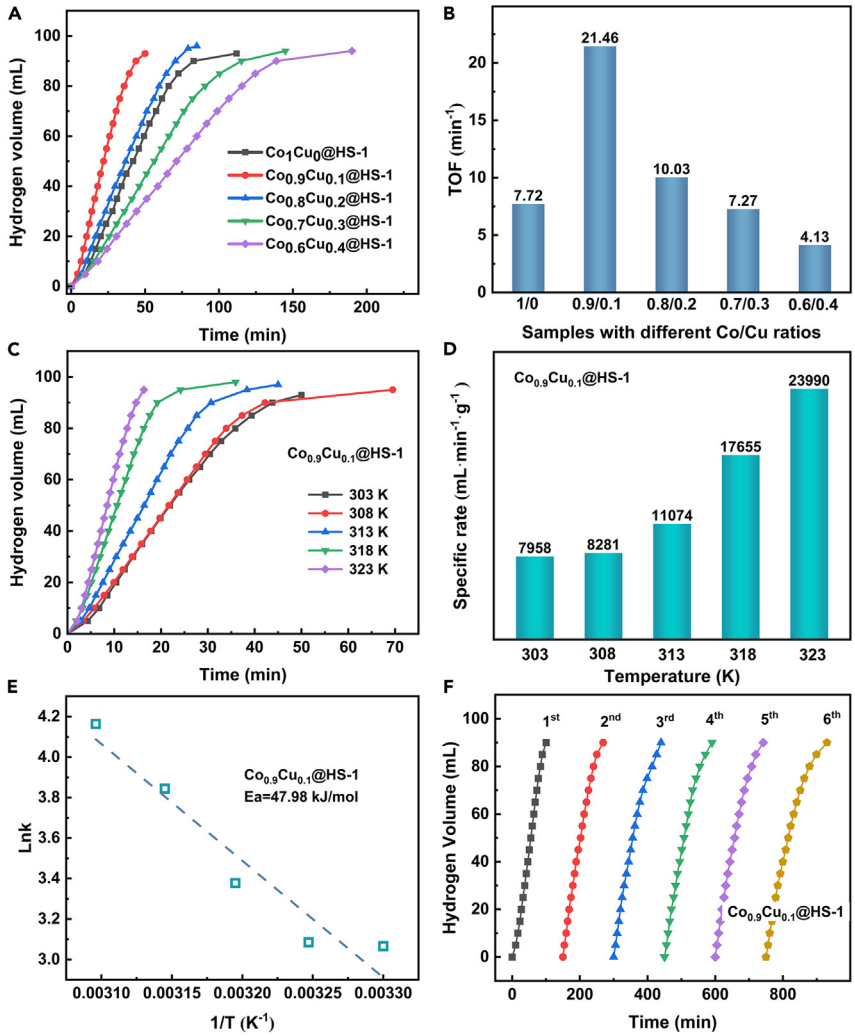

Figure 4. Hydrogen generation properties of NH_3BH_3 hydrolysis catalyzed by Co_xCu_{1-x}@HS-1 samples

(A) Hydrogen generation curves of the NH_3BH_3 hydrolysis catalyzed by Co_xCu_{1-x}@HS-1 samples at 303 K.

(B) TOF value of Co_xCu_{1-x}@HS-1 catalysts.

(C) Hydrogen generation curves for the NH_3BH_3 hydrolysis catalyzed by $Co_{0.9}Cu_{0.1}$@HS-1 at different temperatures.

(D) The corresponding hydrogen generation rates under different temperatures.

(E) The Arrhenius plot and E_a value.

(F) Stability test with $Co_{0.9}Cu_{0.1}$@HS-1 at 303 K.

The specific rate and TOF curves of hydrogen generation catalyzed by Co_xCu_{1-x}@HS-1 samples at 303 K are presented in Figures 4A and 4B. All of Co_xCu_{1-x}@HS-1 samples basically can reach the stoichiometric hydrogen production. Also, the rates of hydrogen production and TOF value increase first with the increase of Cu proportion. When the molar ratio of Co and Cu was 9: 1, the highest TOF value with 21.46 min^{-1} was obtained. As the Cu content continued to increase further, the TOF value of Co_xCu_{1-x}@HS-1 catalyst decreased. The Cu_1Co_0@HS-1 also has no catalytic activity at all for AB hydrolysis. There was an optimal molar value of Co: Cu ratio where the catalytic reaction performance reached the highest point. The catalytic performance results indicated that Co should be the main active component and Cu was electronic additive in the Co_xCu_{1-x}@HS-1. But an appropriate amount of Cu can improve the hydrogen production activity of the catalyst by regulating the electronic property of Co (seen in XPS). Therefore, the synergistic effect between Cu and Co could efficiently improve the catalytic performance for the hydrolytic dehydrogenation of AB in agreement with the literature.[45,46]

Kinetics measurement of $Co_{0.9}Cu_{0.1}$@HS-1 catalyst was studied at various reaction conditions. The reaction of hydrogen generation catalyzed by $Co_{0.9}Cu_{0.1}$@HS-1 at various temperatures indicates that hydrogen production rate increases with temperature (Figure 4C). The apparent activation energy (E_a) is low (47.9 kJ mol^{-1}, Figure 4E), illustrating that the hydrolysis of AB could be easily activated by $Co_{0.9}Cu_{0.1}$@HS-1. Figure 4F exhibits the excellent stability of $Co_{0.9}Cu_{0.1}$@HS-1 catalyst for AB hydrolysis over six cycles. The curves of Figure S4C strongly supports the influence of increased $Co_{0.9}Cu_{0.1}$@HS-1 concentration on hydrogen-generating rate. The logarithmic plots

Table 2. Comparison of $Co_{0.9}Cu_{0.1}$@HS-1 with reported catalysts for NH_3BH_3 Hydrolysis

Catalyst	T/K	TOF	E_a(kJ·mol^{-1})	Reference
$Co_{0.9}Cu_{0.1}$@HS-1	303	21.46	47.98	This work
Co(5)@KD	303	20.05	32.6	Lee et al.[47]
Cu/Zeolite-Y	298	0.78	51.8	Zahmakıran et al.[48]
$Cu_{0.2}Co_{0.8}$/MCM-41	298	15	38	Lu et al.[49]
Co/SAG	303	7.26	46.4	Yu et al.[50]
CoCu/C	298	28.67	51.9	Bulut et al.[51]
Co@M41S	298	10.6	52	Luo et al.[52]
CoO_x-PG	298	3.9	51.3	Wu et al.[53]
Co-CoO_x@GO-II	298	15.3	62.3	Guan et al.[54]
Co−NC/NF_{600}	298	3	64	Mehdi et al.[55]
Co-B/MSP	303	2.77	–	Patel et al.[56]
Co-SBA-5	313	0.35	–	Herron et al.[57]
Co-B/SBA-15	298	4.58	43	Patel et al.[58]
Ni@zeolite	298	5.08	54.4	Zahmakıran et al.[59]

have a positive slope indicating the first-order kinetics in the concentration of $Co_{0.9}Cu_{0.1}$@HS-1 (Figure S4D). Hydrogen-generating rate almost remains unchanged increasing the concentration of AB (Figure S4A). So the hydrolysis of AB and AB concentration were zero-order reaction. Comparision of Co0.9Cu0.1@HS-1 with reported catalysts was shown in Table 2.

Conclusions

In conclusion, Co-Cu NPs uniformly embedded in the intracrystalline mesoporous S-1 have been fabricated successfully by alkali-treatment ligand-assisted methods. The Co_xCu_{1-x}@HS-1 was more efficient in hydrogen production from AB. The $Co_{0.9}Cu_{0.1}$@HS-1 catalyst had the highest hydrogen production efficiency with a TOF value of 21.46 $mol_{H2}\cdot mol_{Me}^{-1}\cdot min^{-1}$ through the optimization study of Co and Cu molar ratio. Activation energy (E_a) was calculated about 47.98 kJ mol^{-1} after the kinetic test. The catalytic activity was maintained after six cycles of stability tests. The Co_xCu_{1-x}@HS-1 prepared by the alkali-treatment ligand-assisted method possess the hierarchical pore structure with the metal particle size of around 2.5 nm. The openness and accessibility of the active sites of Co_xCu_{1-x}@HS-1 have been greatly improved by intracrystalline mesopores, therefore, Co_xCu_{1-x}@HS-1 possess much higher hydrogen production properties than Co_xCu_{1-x}@S-1. The introduction of Cu makes the electron binding energy of Co move higher, further increasing hydrogen production activity. This research introduces a strategy for developing hierarchical porous zeolite-confined metal/metal oxide catalysts, and illustrates the potential of using the metal/metal oxide catalysts in liquid-phase chemical hydrogen storage reaction systems.

Limitations of the study

This study reports that Co-Cu NPs were embedded in the intracrystalline mesoporous Silicalite-1. Intracrystalline mesopores improved the accessibility of the active sites and the introduction of Cu regulates the electronic properties of Co. Future research will focus on the resolution of Co and Cu distribution in zeolite framework using more advanced characterization techniques.

STAR★METHODS

Detailed methods are provided in the online version of this paper and include the following:

- KEY RESOURCES TABLE
- RESOURCE AVAILABILITY
  - Lead contact
  - Materials availability
  - Data and code availability
- EXPERIMENTAL MODEL AND STUDY PARTICIPANT DETAILS
- METHOD DETAILS
  - Preparation of catalysts
  - Characterization of catalysts
  - Catalytic performance in the hydrogen generation by hydrolysis of AB
- QUANTIFICATION AND STATISTICAL ANALYSIS

SUPPLEMENTAL INFORMATION

Supplemental information can be found online at https://doi.org/10.1016/j.isci.2024.109745.

ACKNOWLEDGMENTS

Prof. Baojun Li thanks the financial support from the National Natural Science Foundation of China (No. 22279118). Financial supports from the Key Scientific Research Project of Colleges and Universities in Henan Province (No. 21A530007) are acknowledged. The Center of Advanced Analysis & Gene Sequencing of Zhengzhou University was thanked for XRD and XPS testing.

AUTHOR CONTRIBUTIONS

Conceptualization, B.J.L.; methodology and investigation, Y.N.C. and H.N.H.; writing – original draft, H.J.W.; writing – review and editing, H.J.W., B.J.L., and Y.Y.L.; supervision, X.Y.W. and P.J.; funding acquisition, B.J.L. and Y.Q.W. and X.G.Z.

DECLARATION OF INTERESTS

The authors declare no conflict of interest.

Received: January 12, 2024
Revised: February 27, 2024
Accepted: April 11, 2024
Published: April 15, 2024

REFERENCES

1. Yan, L., Liang, J., Song, D., Li, X., and Li, H. (2024). Modulation of charge redistribution in heterogeneous NiO-Ni_3Se_4 nanosheet arrays for advanced water electrolysis. Adv. Funct. Mater. *34*, 2308345–2308357.
2. Lang, C., Jia, Y., and Yao, X. (2020). Recent advances in liquid-phase chemical hydrogen storage. Energy Storage Mater. *26*, 290–312.
3. Men, Y., Li, P., Yang, F., Cheng, G., Chen, S., and Luo, W. (2019). Nitrogen-doped CoP as robust electrocatalyst for high-efficiency pH-universal hydrogen evolution reaction. Appl. Catal. B Environ. *253*, 21–27.
4. Guan, S., Yuan, Z., Zhuang, Z., Zhang, H., Wen, H., Fan, Y., Li, B., Wang, D., and Liu, B. (2024). Why do single-atom alloys catalysts outperform both single-atom catalysts and nanocatalysts on mxene? Angew. Chem. Int. Ed. *136*, 16550–16560.
5. Feng, Y., Li, Y., Liao, Q., Zhang, W., Huang, Z., Chen, X., Shao, Y., Dong, H., Liu, Q., and Li, H. (2023). Modulation the electronic structure of hollow structured CuO-$NiCo_2O_4$ nanosphere for enhanced catalytic activity towards methanolysis of ammonia borane. Fuel *332*, 126045–126054.
6. Liao, J., Wu, Q., Ye, X., Zhang, T., Li, Y., Ren, J., Liu, Q., Wu, M., and Li, H. (2023). Visible-lightinduced electron density enrichment of the active sites in the core-satellite structured $CuWO_4$@NiO for fast hydrogen generation from ammonia borane methanolysis. Chem. Eng. J. *476*, 146599–146611.
7. Fu, F., Wang, C., Wang, Q., Martinez-Villacorta, A.M., Escobar, A., Chong, H., Wang, X., Moya, S., Salmon, L., Fouquet, E., et al. (2018). Highly selective and sharp volcano-type synergistic Ni_2Pt@ZIF-8-catalyzed hydrogen evolution from ammonia borane hydrolysis. J. Am. Chem. Soc. *140*, 10034–10042.
8. Fang, Y., Xiao, Z., Li, J., Lollar, C., Liu, L., Lian, X., Yuan, S., Banerjee, S., Zhang, P., and Zhou, H.C. (2018). Formation of a highly reactive cobalt nanocluster crystal within a highly negatively charged porous coordination cage. Angew. Chem. Int. Ed. *57*, 5283–5287.
9. Wang, S., Zhang, D., Ma, Y., Zhang, H., Gao, J., Nie, Y., and Sun, X. (2014). Aqueous solution synthesis of Pt–M (M = Fe, Co, Ni) bimetallic nanoparticles and their catalysis for the hydrolytic dehydrogenation of ammonia borane. ACS Appl. Mater. Interfaces *6*, 12429–12435.
10. Shen, R., Liu, Y., Wen, H., Wu, X., Han, G., Yue, X., Mehdi, S., Liu, T., Cao, H., Liang, E., and Li, B. (2022). Engineering bimodal oxygen vacancies and Pt to boost the activity toward water dissociation. Small *18*, 2105588–2105596.
11. Chen, W., Zheng, W., Cao, J., Fu, W., Qian, G., Chen, D., Zhou, X., and Duan, X. (2020). Atomic insights into robust Pt-PdO interfacial site-boosted hydrogen generation. ACS Catal. *10*, 11417–11429.
12. Liao, J., Shao, Y., Feng, Y., Zhang, J., Song, C., Zeng, W., Tang, J., Dong, H., Liu, Q., and Li, H. (2023). Interfacial charge transfer induced dual-active-sites of heterostructured $Cu_{0.8}Ni_{0.2}WO_4$ nanoparticles in ammonia borane methanolysis for fast hydrogen production. Appl. Catal. B Environ. *320*, 121973–121984.
13. Xu, W., Zhang, S., Shen, R., Peng, Z., Liu, B., Li, J., Zhang, Z., and Li, B. (2023). A catalytic copper/cobalt oxide interface for efficient hydrogen generation. Energy Environ. Mater. *6*, 12279–12286.
14. Zang, J.K., Zheng, X.H., Yu, W.L., Feng, X., and Qin, Y. (2022). Unravelling the synergy in platinum-nickel bimetal catalysts designed by atomic layer deposition for efficient hydrolytic dehydrogenation of ammonia borane. Appl. Catal. B Environ. *36*, 121116–121125.
15. Zhang, H., Liu, Y., Zhou, L., Wei, H., Wen, H., Wang, Z., Yue, X., Wu, X., Zhang, Y., Liu, B., et al. (2023). Refined alteration of active sites via O modification on CoP/Co_2P@Carbon hetero-structural catalyst for hydrogen generation. Appl. Catal. B Environ. *325*, 122324–122336.
16. Ji, S., Chen, Y., Zhao, S., Chen, W., Shi, L., Wang, Y., Dong, J., Li, Z., Li, F., Chen, C., et al. (2019). Atomically dispersed ruthenium species inside metal-organic frameworks: combining the high activity of atomic sites and the molecular sieving effect of MOFs. Angew. Chem. Int. Ed. *58*, 4271–4275.
17. Yao, Q., Lu, Z.-H., Yang, Y., Chen, Y., Chen, X., and Jiang, H.L. (2018). Facile synthesis of graphene supported Ni-CeO_x nanocomposites for highly efficient catalysis in hydrolytic dehydrogenation of ammonia borane. Nano Res. *11*, 4412–4422.
18. Zhang, Z., Luo, Y., Liu, S., Yao, Q., Qing, S., and Lu, Z.H. (2019). A PdAg-CeO_2 nanocomposite anchored on mesoporous carbon: highly efficient catalyst for hydrogen production from formic acid at room temperature. J. Mater. Chem. *A. 7*, 21438–21446.
19. Wang, N., Sun, Q., Zhang, T., Mayoral, A., Li, L., Zhou, X., Xu, J., Zhang, P., and Yu, J. (2021). Impregnating subnanometer metallic nanocatalysts into self-pillared zeolite nanosheets. J. Am. Chem. Soc. *143*, 6905–6914.
20. Luo, Y., Yang, Q., Nie, W., Yao, Q., Zhang, Z., and Lu, Z.H. (2020). Anchoring IrPdAu nanoparticles on NH_2-SBA-15 for fast hydrogen production from formic acid at room temperature. ACS Appl. Mater. & Inter. *12*, 8082–8090.
21. Sun, Q., Chen, B.W.J., Wang, N., He, Q., Chang, A., Yang, C.M., Asakura, H., Tanaka, T., Hülsey, M.J., Wang, C.H., et al. (2020). Zeolite-encaged Pd-Mn nanocatalysts for CO_2 hydrogenation and formic acid dehydrogenation. *Angew.* Chem. Int. Ed. *59*, 20183–20191.
22. Otto, T., Zones, S.I., and Iglesia, E. (2018). Synthetic strategies for the encapsulation of nanoparticles of Ni, Co, and Fe oxides within crystalline microporous aluminosilicates. Micro. Meso. Mater. *270*, 10–23.
23. Yan, Y., Zhang, Z., Bak, S.M., Yao, S., Hu, X., Shadike, Z., Do-Thanh, C.L., Zhang, F., Chen, H., Lyu, X., et al. (2019). Confinement of ultrasmall cobalt oxide clusters within Silicalite-1 crystals for efficient conversion of

fructose into methyl lactate. ACS Catal. *9*, 1923–1930.

24. Lee, S., Lee, K., Im, J., Kim, H., and Choi, M. (2015). Revisiting hydrogen spillover in Pt/LTA: Effects of physical diluents having different acid site distributions. J. Catal. *325*, 26–34.
25. Moliner, M., Gabay, J.E., Kliewer, C.E., Carr, R.T., Guzman, J., Casty, G.L., Serna, P., and Corma, A. (2016). Reversible transformation of Pt nanoparticles into single atoms inside high-silica chabazite zeolite. J. Am. Chem. Soc. *138*, 15743–15750.
26. Rasmussen, K.H., Goodarzi, F., Christensen, D.B., Mielby, J., and Kegnæs, S. (2019). Stabilization of metal nanoparticle catalysts via encapsulation in mesoporous zeolites by steam-assisted recrystallization. ACS Appl. Nano Mater. *2*, 8083–8091.
27. Liu, C., Zhang, J., Liu, H., Qiu, J., and Zhang, X. (2019). Heterogeneous ligand-free rhodium oxide catalyst embedded within zeolitic microchannel to enhance regioselectivity in hydroformylation. Ind. Eng. Chem. Res. *58*, 21285–21295.
28. Goel, S., Zones, S.I., and Iglesia, E. (2014). Encapsulation of metal clusters within MFI via interzeolite transformations and direct hydrothermal syntheses and catalytic consequences of their confinement. J. Am. Chem. Soc. *136*, 15280–15290.
29. Liu, L., Díaz, U., Arenal, R., Agostini, G., Concepción, P., and Corma, A. (2017). Generation of subnanometric platinum with high stability during transformation of a 2D zeolite into 3D. Nat. Mater. *16*, 132–138.
30. Zhang, J., Wang, L., Zhang, B., Zhao, H., Kolb, U., Zhu, Y., Liu, L., Han, Y., Wang, G., Wang, C., et al. (2018). Sinter-resistant metal nanoparticle catalysts achieved by immobilization within zeolite crystals via seed-directed growth. Nat. Catal. *1*, 540–546.
31. Jin, Z., Wang, L., Zuidema, E., Mondal, K., Zhang, M., Zhang, J., Wang, C., Meng, X., Yang, H., Mesters, C., and Xiao, F.S. (2020). Hydrophobic zeolite modification for in situ peroxide formation in methaneoxidation to methanol. Science *367*, 193–197.
32. Cui, T.L., Ke, W.Y., Zhang, W.B., Wang, H.H., Li, X.H., and Chen, J.S. (2016). Encapsulating palladium nanoparticles inside mesoporous MFI zeolite nanocrystals for shape-selective catalysis. Angew. Chem. Int. Ed. *55*, 9178–9182.
33. Peng, H., Dong, T., Yang, S., Chen, H., Yang, Z., Liu, W., He, C., Wu, P., Tian, J., Peng, Y., et al. (2022). Intra-crystalline mesoporous zeolite encapsulation-derived thermally robust metal nanocatalyst in deep oxidation of light alkanes. Nat. Commun. *13*, 295–306.
34. Gu, J., Zhang, Z., Hu, P., Ding, L., Xue, N., Peng, L., Guo, X., Lin, M., and Ding, W. (2015). Platinum nanoparticles encapsulated in MFI zeolite crystals by a two-step dry gel conversion method as a highly selective hydrogenation catalyst. ACS Catal. *5*, 6893–6901.
35. Shen, M., Liu, H., Yu, C., Yin, Z., Muzzio, M., Li, J., Xi, Z., Yu, Y., and Sun, S. (2018). Room-temperature chemoselective reduction of 3-nitrostyrene to 3-vinylaniline by ammonia borane over Cu nanoparticles. J. Am. Chem. Soc. *140*, 16460–16463.
36. Guan, S., Zhang, L., Zhang, H., Guo, Y., Liu, B., Wen, H., Fan, Y., and Li, B. (2020). Defect-rich Co-CoO_x-graphene nanocatalysts for efficient hydrogen production from ammonia borane. Chem-Asian J. *15*, 3087–3095.
37. Yang, G., Guan, S., Mehdi, S., Fan, Y., Liu, B., and Li, B. (2021). Co-CoO_x supported onto TiO_2 coated with carbon as a catalyst for efficient and stable hydrogen generation from ammonia borane. Green Energy Environ. *6*, 236–243.
38. Wang, W., Liang, M., Jiang, Y., Liao, C., Long, Q., Lai, X., and Liao, L. (2021). Nano-Co embedded in porous ZIF-67 polyhedron to catalyze hydrolysis of ammonia borane. Mater. Lett. *293*, 129702–129706.
39. Huang, X., Liu, Y., Wen, H., Shen, R., Mehdi, S., Wu, X., Liang, E., Guo, X., and Li, B. (2021). Ensemble-boosting effect of Ru-Cu alloy on catalytic activity towards hydrogen evolution in ammonia borane hydrolysis. Appl. Catal. B Environ. *287*, 119960–119969.
40. Shilina, M.I., Rostovshchikova, T.N., Nikolaev, S.A., and Udalova, O.V. (2019). Polynuclear Co-oxo cations in the catalytic oxidation of CO on Co-modified ZSM-5 zeolites. Mater. Chem. Phys. *223*, 287–298.
41. Liotta, L., Pantaleo, G., Macaluso, A., Carlo, G.D., and Deganello, G. (2003). CoO_x catalysts supported on alumina and alumina-baria: influence of the support on the cobalt species and their activity in NO reduction by C_3H_6 in lean conditions. Appl. Catal. A: Gen. *245*, 167–177.
42. Vandewater, L., Bezemer, G., Bergwerff, J., Versluijs-Helder, M., Weckhuysen, B., and Dejong, K. (2006). Spatially resolved UV–vis microspectroscopy on the preparation of alumina-supported Co Fischer–Tropsch catalysts: Linking activity to Co distribution and speciation. J. Catal. *242*, 287–298.
43. Yan, J., Kung, M.C., Sachtler, W.M., and Kung, H.H. (1997). Co/Al_2O_3 Lean NO_x Reduction Catalyst. J. Catal. *172*, 178–186.
44. Kang, B., Zhang, R., Guo, M., Guo, X., Di, Z., Wei, Y., and Jia, J. (2023). Topological aspect of the distribution of Co species and N_2O decomposition performance for Co/Zeolite catalysts. Energy Fuels *37*, 18019–18029.
45. Song, F.Z., Zhu, Q.L., Yang, X.C., and Xu, Q. (2016). Monodispersed CuCo nanoparticles supported on diamine-functionalized graphene as a non-noble metal catalyst for hydrolytic dehydrogenation of ammonia borane. ChemNanoMat *2*, 942–945.
46. Zhang, F., Li, R., Zhang, J., and Dong, H. (2022). KCC-1 Supported CuCo bimetal catalysts for promoting hydrogen production from ammonia borane hydrolysis. Catal. Lett. *152*, 2832–2839.
47. Lee, M.H., Deka, J.R., Cheng, C.J., Lu, N.F., Saikia, D., Yang, Y.C., and Kao, H.M. (2019). Synthesis of highly dispersed ultra-small cobalt nanoparticles within the cage-type mesopores of 3D cubic mesoporous silica via double agent reduction method for catalytic hydrogen generation. Appl. Surf. Sci. *470*, 764–772.
48. Zahmakıran, M., Durap, F., and Özkar, S. (2010). Zeolite confined copper(0) nanoclusters as cost-effective and reusable catalyst in hydrogen generation from the hydrolysis of ammonia-borane. Int. J. Hydrogen Energy *35*, 187–197.
49. Lu, Z.H., Li, J., Feng, G., Yao, Q., Zhang, F., Zhou, R., Tao, D., Chen, X., and Yu, Z. (2014). Synergistic catalysis of MCM-41 immobilized Cu–Ni nanoparticles in hydrolytic dehydrogeneration of ammonia borane. Int. J. Hydrogen Energy *39*, 13389–13395.
50. Yu, P.J., Lee, M.H., Hsu, H.M., Tsai, H.M., and Chen-Yang, Y.W. (2015). Silica aerogel-supported cobalt nanocomposites as efficient catalysts toward hydrogen generation from aqueous ammonia borane. RSC Adv. *5*, 13985–13992.
51. Bulut, A., Yurderi, M., Ertas, İ.E., Celebi, M., Kaya, M., and Zahmakiran, M. (2016). Carbon dispersed copper-cobalt alloy nanoparticles: A cost-effective heterogeneous catalyst with exceptional performance in the hydrolytic dehydrogenation of ammonia-borane. Appl. Catal. B Environ. *180*, 121–129.
52. Luo, Y.C., Liu, Y.H., Hung, Y., Liu, X.Y., and Mou, C.Y. (2013). Mesoporous silica supported cobalt catalysts for hydrogen generation in hydrolysis of ammonia borane. Int. J. Hydrogen Energy *38*, 7280–7290.
53. Wu, X., Zhang, X., Han, G., Liu, Y., Liu, B., Gao, J., Fan, Y., and Li, B. (2018). Reaction of Co_3O_4 nanocrystals on graphene sheets to fabricate excellent catalysts for hydrogen generation. ACS Sustain. Chem. Eng. *6*, 8427–8436.
54. Guan, S., Zhang, L., Zhang, H., Guo, Y., Liu, B., Wen, H., Fan, Y., and Li, B. (2020). Defect-rich Co-CoOx -graphene nanocatalysts for efficient hydrogen production from ammonia borane. Chem. Asian J. *15*, 3087–3095.
55. Mehdi, S., Liu, Y., Wei, H., Wen, H., Shen, R., Peng, Z., Zhang, H., Wu, X., Wang, C., Guan, S., et al. (2022). Co-based nanoparticles fabricated on Ni foams for efficient hydrogen generation from ammonia borane. ACS Appl. Nano Mater. *5*, 5064–5074.
56. Patel, N., Fernandes, R., Edla, R., Lihitkar, P.B., Kothari, D.C., Miotello, A., and Miotello, A. (2012). Superior hydrogen production rate by catalytic hydrolysis of ammonia borane using Co-B nanoparticles supported over mesoporous silica particles. Catal. Commun. *23*, 39–42.
57. Herron, R., Marchant, C., and Sullivan, J.A. (2018). Co-SBA-15 catalysts in the hydrolysis of NH_3BH_3 - Influences of Co precursors and catalyst pre-treatment. Catal. Commun. *107*, 14–17.
58. Patel, N., Fernandes, r., Gupta, S., Edla, R., Kothari, D.C., and Miotello, A. (2013). Co-B catalyst supported over mesoporous silica for hydrogen production by catalytic hydrolysis of Ammonia Borane: A study on influence of pore structure. Appl. Catal. B Environ. *140–141*, 125–132.
59. Zahmakıran, M., Ayvalı, T., Akbayrak, S., Çalışkan, S., Çelik, D., and Özkar, S. (2011). Zeolite framework stabilized nickel(0) nanoparticles: Active and long-lived catalyst for hydrogen generation from the hydrolysis of ammonia-borane and sodium borohydride. Catal. Today *170*, 76–84.

STAR★METHODS

KEY RESOURCES TABLE

REAGENT or RESOURCE	SOURCE	IDENTIFIER
Chemicals, peptides, and recombinant proteins		
Tetraethoxysilane (TEOS), 28.4 wt%	Sinopharm Group Chemical Reagent Co., Ltd.	CAS: 562-90-3
Tetrapropylammonium hydroxide (TPAOH), 25 wt%	Beijing Xingfu Institute of Fine Chemistry	CAS: 4499-86-9
Cobalt nitrate ($Co(NO_3)_2 \cdot 6H_2O$), AR, 99%	Shanghai Maclin Biochemical Co., Ltd.	CAS: 10026-22-9
Copper nitrate ($Cu(NO_3)_2 \cdot 3H_2O$), AR, 99%	Shanghai Maclin Biochemical Co., Ltd.	CAS: 3251-23-8
Tetrapropylammonium bromide (TPABr), AR, 98%	Shanghai Maclin Biochemical Co., Ltd.	CAS: 1941-30-6
N-(2-aminoethyl)-3-aminopropyltrimethoxysilane (TPE), AR, 95%	Shanghai Aladdin Biochemical Technology Co., Ltd.	CAS: 1760-24-3
Ethanolamine (ETA), AR, 99%	Sinopharm Group Chemical Reagent Co., Ltd.	CAS: 141-43-5
Ammonia borane, AR, 99%	Beijing Yinokai Technology Co., Ltd.	CAS: 13774-81-7
Alcohol, AR	Tianjin Fengboat Chemical Reagent Technology Co., Ltd.	CAS: 64-17-5

RESOURCE AVAILABILITY

Lead contact

Further information and requests for resources should be directed to and will be fulfilled by the lead contact, Professor Baojun Li (lbjfcl@zzu.edu.cn).

Materials availability

The study did not generate new unique materials. The readers can buy the chemicals to remake the materials as mentioned in the text.

Data and code availability

Data: All data reported in this paper will be shared by the lead contact upon request.
Code: This paper does not report the original code.
Any additional information required to reanalyze the data reported in this paper is available from the lead contact upon request.

EXPERIMENTAL MODEL AND STUDY PARTICIPANT DETAILS

This study does not use experimental models.

METHOD DETAILS

Preparation of catalysts

Synthesis of Silicalite-1 (S-1): The nanosized silicalite-1 zeolite crystals were synthesized under conventional hydrothermal conditions at 170°C for 48 h from the starting gel with the molar composition of 1.0 SiO_2: 0.2 TPAOH: 20 H_2O. Typically, 15.6 g TPAOH solution (25 wt%) was first mixed with the deionized water. Then, 20 g TEOS was dropwise added into the above mixture. The obtained solution was stirred at room temperature for 3 h to make the solution clear. The solution was heated at 70°C to remove alcohol for 2 h, and then stirred to age at 45°C for 24 h. After the aging, the mixed solution was put into a Teflon-lined stainless-steel autoclave and crystallized at 170°C for 48 h. The as-synthesized solid products were then separated by centrifugation, washed by deionized water for several times, then dried at 80°C overnight, and finally calcined in a 550°C muffle furnace for 6 h.

Synthesis of Cobalt-Copper@Silicalite-1 (Co_xCu_{1-x}@S-1): Co_xCu_{1-x}@S-1 was prepared by *in-situ* ligand-assisted method. A solution was obtained by adding the metal precursor solution (a certain amount of $Co(NO_3)_2 \cdot 6H_2O$ and $Cu(NO_3)_2 \cdot 3H_2O$ was dissolved in 5 mL H_2O and the total molar amount of metal was 2.25 mmol) drop by drop to TPE protector solution (1 g TPE was dissolved in 5 mL H_2O). B solution was obtained by mixing TEOS, TPAOH and water according to the molar composition of 1.0 SiO_2: 0.2 TPAOH: 20 H_2O. Then A solution was added to B solution slowly under the stirring. The final obtained gels were aged at 45°C for 24 h and crystallized at 170°C for 48 h. The solid product was separated by centrifugation, washed by deionized water for four times, dried overnight at 80°C and calcined in a muffle furnace at 550°C for 6 h under nitrogen atmosphere.

Synthesis of Cobalt-Copper@ Hierarchical-Silicalite-1 (Co_xCu_{1-x}@HS-1): Co_xCu_{1-x}@HS-1 was prepared by ligand-assisted alkali treatment method. The S-1 was first prepared according to the synthesis of S-1 in the experiment section. The metal precursor solution was prepared by dropwise adding the aqueous solution of $Co(NO_3)_2 \cdot 6H_2O$ and $Cu(NO_3)_2 \cdot 3H_2O$ (2.25 mmol of total metal in 5 mL H_2O) to the aqueous TPE

solution (1 g TPE was dissolved in 5 mL H_2O) under the stirring with a magnetic bar. The S-1 were hydrothermally post-treated with the mixed solution of ETA, TPABr and metal precursor solution according to the molar ratio with 1.0 S-1: 0.66 ETA: 0.6 TPABr: 0.00225 metal (Cu and Co): 22.3 H_2O at 170°C for 48 h. The as-synthesized solid products were then separated by centrifugation, washed several times with pure water, then dried at 80°C overnight, and finally calcined in a 550°C muffle furnace for 6 h under nitrogen atmosphere.

Characterization of catalysts

X-ray diffraction (XRD) were recorded on a Panalytical X'pert PRO diffraction-meter (40 kV, 40 mA) using Cu Kα radiation source (λ = 1.540598 Å) at a scanning step of 1.2° min^{-1} in the 2θ range from 4° to 80°. N_2 adsorption-desorption isotherms were measured using Micromeritics ASAP-2420 analyzer at 77 K. Prior to N_2 adsorption, all of the samples were evacuated under a vacuum for 3 h at 423K. Brunauer-Emmett-Teller (BET) method was adopted to calculate the total surface area (S_{BET}). Total pore volume (V_{tot}) was determined by a single point method from the volume adsorbed at p/p_0 = 0.95. The micropore surface area (S_{mic}), external surface area (S_{ext}) and the micropore volume (V_{mic}) was calculated by the t-plot method. The elementary composition was measured by inductively Coupled Plasma Optical Emission Spectrometer Agilent 5110 (ICP). Transmission electron micrographs (TEM) were taken on a FEI Tecnai G^2 F20 X-Twin electron microscopes operating at 200 kV. XPS was collected on a Thermo Scientific Escalab Xi+ with an Al Kα = 1486.60 eV and the binding energies were calibrated by referencing the C 1s peak (284.8 eV) to reduce the sample charge effect.

Catalytic performance in the hydrogen generation by hydrolysis of AB

The amount of hydrogen evolution by hydrolysis of AB was determined by the drainage gas collection method. The catalyst (10 mg) finely grounded is mixed with 2 mL deionized water. AB (45 mg) was dissolved in 3 mL deionized water. The two solutions were dispersed by ultrasonic for 1 min respectively. 25 mL round bottom flask was placed in a thermostatic water bath at 25°C with a self-stirring speed of 500 rpm. In addition, a water-filled measuring cylinder is placed upside down in the container to record the volume of hydrogen. Firstly, catalyst dispersion was added into the round bottom flask and then the aqueous AB solution was again quickly poured into the round bottom flask. The time started when the second bubble was generated and data was recorded each 5 mL hydrogen. In the cyclic stability test of catalyst, the experimental procedures were the same as above. After the first experiment on hydrogen production by hydrolysis of ammonia borane, then the new equal amount of AB was directly added to the reaction system, and the volume of hydrogen produced was tested in the same way without treating the catalyst in any way. This operation is repeated until the cyclic stability test is over. In order to explore the kinetics of the reaction system, the experiments on hydrogen production were carried out at different reaction temperatures and the experimental procedures were the same as above.

The data of the whole stabilization phase of the reaction are used to calculate the rate of hydrogen generation r_B and TOF value according to the following two formulas:

$$r_B = \frac{50}{[t_{75} - t_{25}]w_{cat}}$$

$$TOF = \frac{n_{H_2}}{n_{cat}[t_{75} - t_{25}]}$$

t_{75} represent the time required to produce 75 mL hydrogen, t_{25} represent the time required to produce 25mL hydrogen, w_{cat} denotes the mass of the active component in the catalyst, n_{H2} is the number of moles of H_2 produced during the hydrogen produced volume from 25 to 75 mL, n_{cat} indicates the molar amount of active component in the catalyst.

QUANTIFICATION AND STATISTICAL ANALYSIS

This study does not include statistical analysis or quantification.